Stable isotope fractionation reveals similar atomic level controls during aerobic and anaerobic microbial Hg transformation pathways

Running title: Isotopes unify controls on bacterial Hg transformations

Daniel S. Grégoire [a*#], Sarah E. Janssen [b], Noémie C. Lavoie [a], Michael T. Tate [b], & Alexandre J. Poulain [a]

a - Biology Department, University of Ottawa, 30 Marie Curie, Ottawa, ON, K1N 6N5, Canada.

b - Upper Midwest Water Science Center, U.S. Geological Survey, Middleton, Wisconsin 53562, USA.

Corresponding author: Dr. Daniel S. Grégoire, daniel.gregoire@uwaterloo.ca

* Current affiliation: Biology Department, University of Waterloo, 200 University Ave W, Waterloo, ON, N2L 3G1

Word count for abstract: 248

Word count for text (excluding abstract and importance sections, including captions): 6074

Any use of trade, firm, or product names is for descriptive purposes only and does not imply endorsement by the U.S. Government

ABSTRACT

Mercury (Hg) is a global pollutant and potent neurotoxin that bioaccumulates in food webs as monomethylmercury (MeHg). The production of MeHg is driven by anaerobic and Hg redox cycling pathways such as Hg reduction, which control the availability of Hg to methylators. Anaerobes play an important role in Hg reduction in methylation hotspots, yet their contributions remain underappreciated due to how challenging these pathways are to study in the absence of dedicated genetic targets and low levels of Hg^0 in anoxic environments. In this study we used Hg stable isotope fractionation to explore Hg reduction during anoxygenic photosynthesis and fermentation in the model anaerobe *Heliobacterium modesticaldum* Ice1. We show that cells preferentially reduce lighter Hg isotopes in both metabolisms leading to mass-dependent fractionation, but mass-independent fractionation commonly induced by UV-visible light is absent. Due to variability associated with replicated experiments, we could not discern whether dedicated physiological processes drive Hg reduction during photosynthesis and fermentation. However, we demonstrate that fractionation is affected by the interplay between pathways controlling Hg recruitment, accessibility, and availability alongside metabolic redox reactions. The combined contributions of these processes lead to isotopic enrichment during anoxygenic photosynthesis that is in between the values reported for anaerobic respiratory microbial Hg reduction and abiotic photoreduction. Isotope enrichment during fermentation is closer to what has been observed in aerobic bacteria that reduce Hg through dedicated detoxification pathways. Our work suggests that similar controls likely underpin diverse microbe-mediated Hg transformations that affect Hg's fate in oxic and anoxic habitats.

45 **IMPORTANCE**

46 Anaerobic and photosynthetic bacteria that reduce mercury affect mercury delivery to microbes
47 in methylation sites that drive bioaccumulation in food webs. Anaerobic mercury reduction
48 pathways remain underappreciated in the current view of the global mercury cycle because they
49 are challenging to study, bearing no dedicated genetic targets to establish physiological
50 mechanisms. In this study we used stable isotopes to characterize the physiological processes
51 that control mercury reduction during photosynthesis and fermentation in the model anaerobe
52 *Heliobacterium modesticaldum* Ice1. The sensitivity of isotope analyses highlighted the subtle
53 contribution of mercury uptake towards the isotope signature associated with anaerobic mercury
54 reduction. When considered alongside the isotope signatures associated with microbial pathways
55 for which genetic determinants have been identified, our findings underscore the narrow range of
56 isotope enrichment that is characteristic of microbial mercury transformations. This suggests that
57 there exist common atomic-level controls for biological mercury transformations across a broad
58 range of geochemical conditions.

59

60 **INTRODUCTION**

61 Mercury (Hg) is a global pollutant and potent neurotoxin that bioaccumulates in aquatic and
62 terrestrial food webs as monomethylmercury (MeHg) (1). Anaerobic microbes with the *hgcAB*
63 gene cluster, which encodes for the metabolic machinery responsible for Hg methylation (2),
64 contribute to MeHg production in habitats such as aquatic sediments, water columns, and
65 flooded soils (3-6). Hg methylation is thought to occur intracellularly and as such, it is ultimately
66 controlled by the bioavailability of Hg to methylators in anoxic habitats (7).

67 Hg redox cycling plays a key role in determining the inorganic Hg substrates available to
68 methylators. Its role is two-fold: anaerobic Hg^0 oxidation can supply dissolved Hg^{II} required to
69 generate MeHg and evasion of Hg^0 due to reduction can limit MeHg production by removing
70 inorganic Hg substrates. Although it is well established that abiotic photochemical Hg reduction
71 dominates Hg redox cycling in oxic surface systems where light is present (8-16), Hg reduction
72 pathways in anoxic zones where Hg methylation occurs have mostly been characterized under
73 laboratory conditions and remain challenging to assess in the field.

74 Anoxic Hg reduction can occur via abiotic redox reactions with dissolved organic carbon
75 (17) and magnetite (18, 19), but also through biotic pathways mediated by chemotrophic and
76 phototrophic microorganisms (20-24). Unlike many aerobes that reduce Hg using dedicated
77 enzymatic machinery encoded by the *mer* operon (25, 26), Hg reduction in anaerobes occurs
78 through cometabolic pathways tied to anaerobic respiration, fermentation, and anoxygenic
79 photosynthesis (20-24). In contrast to *mer*-mediated Hg reduction and demethylation, dedicated
80 genetic determinants have yet to be identified for anaerobic Hg reduction, making these
81 pathways challenging to study from a mechanistic standpoint. Furthermore, while some studies
82 have shown that Hg^0 can significantly contribute to Hg speciation in anoxic habitats (27, 28), it is

83 possible that low levels of Hg^0 are maintained by an active cycle of reduction and oxidation (29).
84 In the absence of genetic targets and measurable Hg^0 accumulation, the contributions of
85 anaerobic Hg^0 production to global Hg cycling remain cryptic and difficult to assess.
86 The use of stable Hg isotope fractionation is a powerful tool for providing
87 biogeochemical proxies for different abiotic and biotic Hg transformations (30, 31). All abiotic
88 and biotic Hg transformation pathways studied to date demonstrate kinetic mass dependent
89 fractionation (MDF) in which the product pool becomes isotopically lighter (enrichment of light
90 isotopes) as the reaction proceeds (32). Some pathways, such as abiotic photochemical reduction
91 and demethylation, also demonstrate mass independent fractionation (MIF), which is defined as
92 fractionation that occurs outside of the predicted MDF pattern (30). MIF is most commonly
93 observed due to the magnetic isotope effect for odd-Hg isotopes ^{199}Hg and ^{201}Hg in the presence
94 of sunlight (33) and the extent to which MIF occurs is controlled in part by water chemistry and
95 the presence of photosynthetic organisms (39).
96 The combination of MDF and MIF tracers, and the rate of isotopic enrichment, referred
97 to as fractionation factor, can be used to outline the underlying components of different microbe-
98 mediated Hg transformation pathways. Over the last decade, Hg isotope fractionation has been
99 studied in microbes capable of *mer*-mediated reduction (34) and MeHg demethylation (35);
100 anaerobic non-*mer*-mediated Hg reduction (36, 37); Hg methylation (37-40); and oxygenic
101 phototrophic MeHg degradation and Hg reduction (41). These studies have yielded valuable
102 insights and mechanistic details that explain how microbes interact with Hg at the atomic level
103 making them a promising option for studying mechanisms for anaerobic Hg reduction.
104

105 Our objective in this study was to characterize Hg isotope fractionation patterns during
106 anoxygenic phototrophic and fermentative Hg^{II} reduction, for which there exists no data. By
107 providing the first isotopic characterization of these pathways we aim to better understand the
108 underlying physiological pathways involved in anaerobic Hg reduction and their role in
109 controlling Hg availability to methylators in anoxic habitats.

110 In this work, we test whether Hg reduction by the model anaerobe *Heliobacterium*
111 *modesticaldum* Ice1 during anoxygenic photosynthesis and fermentation leads to distinct isotope
112 enrichment signatures, which would suggest the different metabolic Hg reduction pathways are
113 controlled by separate processes. We chose to work with this model Heliobacteria because its
114 metabolic versatility is representative of the strategies that allow this family to thrive in the same
115 niche as methylators in habitats such as rice paddies where MeHg accumulation is a major health
116 concern (42-45). Furthermore, our previous work showed that *H. modesticaldum* has the capacity
117 to reduce high proportions of Hg^{II}, making this strain well-suited to producing the high levels of
118 Hg^0 required for measuring isotope fractionation (23). In addition to comparing isotope
119 fractionation associated with different metabolic pathways in *H. modesticaldum*, we compare the
120 isotope enrichment observed in this study to previously published isotope signatures for biotic
121 and abiotic Hg transformations to critically evaluate whether common controls exist for microbe-
122 mediated Hg transformations. Finally, we discuss whether current analytical capacity for isotope
123 fractionation can be used to track the contributions of such pathways in the environment.
124

125 # METHODS

126 **Cell growth conditions and bioreactor setup**

127 All experiments with live cells employed the strain *Heliobacterium modesticaldum* Ice1 grown
128 in PYE medium. PYE medium was prepared by dissolving the following ingredients in 1 L of
129 ultra-filtered high purity (18.2 MΩ) water: Dipotassium phosphate (K_2HPO_4) (1 g L^{-1});
130 magnesium sulphate heptahydrate ($MgSO_4$ x $7H_2O$) (0.2 g L^{-1}); calcium chloride dihydrate
131 ($CaCl_2$ x $2H_2O$) (0.02 g L^{-1}); sodium thiosulphate pentahydrate ($Na_2S_2O_3$) x $5H_2O$ (0.2 g L^{-1});
132 sodium pyruvate (2.20 g L^{-1}); yeast extract (YE) (4.00 g L^{-1}); and ammonium sulphate
133 [$(NH_4)_2SO_4$] (1.00 g L^{-1}). The pH of the medium was adjusted to 6.8, after which 1 mL of a
134 filter-sterilized (0.2 µm pore size) trace element solution was added to the medium as a 1000X
135 dilution. The trace element stock was prepared by adding the following ingredients to 1 L of
136 ultra-filtered high purity water: Zinc sulphate heptahydrate ($ZnSO_4$ x $7H_2O$) (0.10 g L^{-1});
137 manganese chloride tetrahydrate ($MnCl_2$ x $4H_2O$) (0.03 g L^{-1}); boric acid (H_3BO_3) (0.30 g L^{-1});
138 cobalt chloride hexahydrate ($CoCl_2$ x $6H_2O$) (0.20 g L^{-1}); cupric chloride dihydrate ($CuCl_2$ x
139 $2H_2O$) (0.01 g L^{-1}); nickel chloride hexahydrate ($NiCl_2$ x $6H_2O$) (0.02 g L^{-1}); sodium molybdate
140 dihydrate (Na_2MoO_4 x $2H_2O$) (0.03 g L^{-1}). The medium was then boiled for 15 minutes under a
141 stream of sterile nitrogen (N_2) gas before being aliquoted to serum bottles or balch tubes that
142 were crimped shut, flushed with N_2 gas, and autoclaved at 121°C for 30 min.

143 Phototrophic cultures were grown at a constant visible light intensity of 80 µmol photon
144 m^{-2} s^{-1} with a peak irradiance in the near-red to red spectrum (600 nm to 700 nm) at 50°C
145 whereas fermentative cultures were grown in the dark at 50°C in line with our previous work
146 (23). *H. modesticaldum* Ice1 was obtained from the Leibniz Institute Deutsche Sammlung von
147 Mikroorganismen und Zellkulturen (DSMZ) culture collection (catalogue number DSM-792).

148 The bioreactor methodology employed in these experiments was similar to the one used in
149 previous work (23) with the following modifications: The bioreactor was periodically supplied
150 with sterile N_2 gas that passed through an activated carbon filter and a 0.2 µm pore size air filter
151 at a flow rate of 0.25 L min^{-1} and two gold traps were connected in series at the reactor outlet to
152 capture Hg^0 (**Fig S1**).

153 The bioreactor was kept in an incubator set to 50°C. Phototrophic experiments were
154 performed using a 60 W incandescent light bulb with a visible light intensity being maintained at
155 20 µmol photon m^{-2} s^{-1} and mirroring the irradiance of growth conditions. Fermentative
156 experiments were performed in the dark. Background Hg^0 was purged and removed from
157 reactors prior to phototrophically or fermentatively-grown *H. modesticaldum* cells being added
158 as a 10 % (v/v) inoculum after which an additional subsample was withdrawn to verify initial
159 cell density via O.D. 600 nm. For sterile treatments, no cells were added to the bioreactor and the
160 volume of growth medium was adjusted to ensure experiments were carried out at a working
161 volume of 500 mL. We chose to use sterile medium rather than heat-killed cultures based on our
162 previous work, which showed that autoclaved cultures of *H. modesticaldum* supplied with Hg^{II}
163 under the same conditions reduced negligible amounts of Hg^{II} (23). In all experiments, National
164 Institute of Standards and Technology (NIST) 3133, a standard with certified Hg isotope values,
165 was added to the bioreactor to approximately 10 nM Hg final concentration. Additional details
166 on the bioreactor setup are provided in **Supporting Methods**.

167

168 **Hg^0 measurements**

169 The bioreactor was bubbled periodically rather than continuously in contrast to previous work
170 because continuous bubbling led to fouling of gold traps and poor total Hg (THg) and isotope
171 recoveries. Subsamples were collected at designated timepoints by connecting dual gold traps to
172 the reactor and purging the reactor for 30 min to collect Hg^0. In the final 5 mins, the reactor
173 liquid was sampled for Hg^{II} concentration, isotopic composition, and cell growth after which gas
174 flow was stopped. All gold traps were capped to prevent Hg^0 loss and aqueous samples were
175 conserved with 1% (v/v) trace element grade hydrochloric acid (HCl) at 4°C in the dark. Reactor
176 washes were performed using trace element grade HCl following previously established
177 protocols (23).

178

179 **Total Hg analyses and sample preparation for stable isotope measurements**

180 All samples for aqueous Hg analyses were oxidized with 10 % (v/v) bromine chloride (BrCl) in
181 line with previous work (40). THg concentrations were determined by stannous chloride
182 reduction coupled to cold vapor atomic fluorescence spectrometry at the U.S. Geological Survey
183 Mercury Research Lab (USGS MRL, Middleton, WI) (46). During THg analysis, duplicates and
184 matrix standard spikes were analyzed every 10 samples; analyses showed less than 10 % relative
185 percent difference between duplicates and spike recoveries of 90-110%. The detection limit was
186 0.2 pM.

187 Total Hg mass balances were calculated in line with previous work (23, 24) with
188 corrections to account for the mass of Hg removed for each subsample. For Hg^0 collected onto
189 gold traps, a thermal desorption system was used to liberate Hg^0 over a 40 min desorption cycle
190 which was then captured in 40% nitric acid (HNO_3):BrCl (3:1) oxidizing solution. An aliquot of

191 the trapping solution was subsequently analyzed for THg concentration following the protocol
192 established in previous work (47). Desorption efficiency during pre-concentration was tested by
193 trapping a NIST 3133 standard with each batch of samples, and recoveries for standard trapping
194 were 101.27 ± 4.26 % (n = 15). THg recoveries from bioreactor experiments were 94.90 ± 9.50
195 % (n=7) (**Fig S2**).
196

197 **Hg stable isotope analyses**

198 Using the previously determined THg concentration, an aliquot of the trapping solution was
199 diluted with ultra-high purity water to an acid content < 10% H^+ and a THg concentration of 3.75
200 to 5.00 nM (48). A Neptune Plus multicollector-inductively coupled plasma mass spectrometer
201 (MC-ICP-MS, Thermo Scientific) was used for Hg stable isotope ratio measurements at the
202 USGS MRL. A concentration and matrix-matched NIST 3133 Hg standard was used for sample
203 bracketing (49). To achieve detection at low Hg concentrations, Hg was reduced with stannous
204 chloride in-line then introduced continuously into a custom designed gas liquid separator along
205 with a thallium standard (NIST SRM 997, 195 nM in 3% HCl) for mass bias correction (48, 50).
206 MC-ICP-MS instrument conditions and analytical expectations were derived from previously
207 published work. All quality control metrics for Hg stable isotope analysis and raw data are
208 provided in **Supporting Methods, Table S1** and **Table S2**. Note that very low levels of Hg^0
209 were produced in abiotic controls for both phototrophic and fermentative experiments and as
210 such there was insufficient Hg^0 to measure isotope fractionation in the product pool (**Table S2**).
211

212 **Isotope calculations**

213 Delta calculations followed the conventions set forth by others (49). This convention calls for
214 mass dependent fractionation (MDF) to be expressed in terms of δ^{xxx}Hg where graphically
215 δ^{202}Hg is used to signify MDF. δ^{xxx}Hg is calculated as:

216 $$\delta^{xxx}\text{Hg}(‰) = [(^{xxx}\text{Hg}/^{198}\text{Hg}_{sample})/(^{xxx}\text{Hg}/^{198}\text{Hg}_{NIST\text{-}3133}) - 1]\times 1000. \quad (\textbf{Eq 1})$$

217 XXX is used to signify the isotope of interest. Hg also undergoes MIF of both even and odd
218 isotopes. Here, odd-MIF is described by Δ^{199}Hg and even-MIF by Δ^{200}Hg. MIF is calculated as:

219 $$\Delta^{xxx}\text{Hg} \approx \delta^{xxx}\text{Hg} - (\delta^{202}\text{Hg} * \beta). \quad (\textbf{Eq 2})$$

220 β denotes the mass dependent scaling constant, which is determined by the laws of mass
221 dependence (49). Isotope enrichment effects based on the ratio of products to reactants (i.e. $\varepsilon_{p/r}$,
222 herein referred to as ε_{AP} for anoxygenic phototrophic reduction and ε_{FM} for fermentative
223 reduction) were calculated using Rayleigh fractionation models to account for the Hg^0 that was
224 removed following methods from previous work on microbial Hg reduction (34). This method
225 involved fitting a linear regression (shown in **Fig S3, Fig S4,** and **Table S3**) based on the change
226 in relative isotope ratios, $\ln(R/R_0)$, as a function of $\ln(f_r)$ where:

227 $R = (\delta^{202}\text{Hg}/1000) + 1$ for Hg^{II} (reactant) or Hg^0 (product) at a given time point and
228 $R_0 = (\delta^{202}\text{Hg}/1000) + 1$ at the beginning of the experiment (**Eq 3**);

229 f_r= Hg^{II} in the reactor at a given time / Hg^{II} in the reactor at the start of the experiment (**Eq 4**);
230 and the slope of the linear regression, which is equivalent to ε_{AP} or ε_{FM}:

231 $$\varepsilon = \ln(R/R_0)/\ln(f_r) \quad (\textbf{Eq 5}).$$

232 We chose to use the total Hg analyses from the bioreactor to establish f_r as this is a true
233 representation of the instantaneous isotope fractionation rather than a time integrated sample
234 following the methods outlined in previous work (34). Note that in our slope calculations we do

235 not have data for $^{202}Hg^0$ when f_r=1 (the 0h sampling point) because no isotope fractionation was
236 taking place prior to the start of Hg reduction (**Table S2** and **Table S3**). Additionally, in
237 experiments where negligible amounts of Hg^{II} were reduced to Hg^0, data points for $\delta^{202}Hg$ in the
238 Rayleigh fractionation plots tend to cluster around to f_r = 1 since ~100% of the original Hg
239 supplied remained in the reactor after 48 hours. Additional calculations for isotope mass balances
240 were carried out to test for deviation from the Rayleigh model and can be found in **Table S4.**
241 ε values for MDF were compiled from previous studies on pure microbial cultures and
242 abiotic Hg transformations for comparison purposes. Currently, there is no standard guideline for
243 how to calculate ε and studies vary widely in how they present isotope enrichment data and their
244 associated variability. We have provided details on how we normalized ε values from different
245 studies in **Table S5**. In this work we only compared enrichment factors from studies that used
246 MC-ICP-MS techniques and slope calculations in line with our analyses, however we have
247 included all of the ε values for microbe-driven Hg transformations published to date in **Table S5**.
248
249
250 ## RESULTS AND DISCUSSION

251 **Hg^0 production during anoxygenic photosynthesis and fermentation**

252 In our experiments Hg^0 production relied on the presence of live cells for both fermentative and
253 phototrophic growth conditions. Cumulative Hg^0 production was an order of magnitude higher
254 for live cell treatments compared to abiotic controls (>0.60 vs <0.05 nmol) (**Fig 1**). Fermentative
255 cells produced double the amount of Hg^0 compared to phototrophic cells (1.33 to 1.64 nmol vs
256 0.60 to 0.81 nmol, respectively) despite having been supplied with slightly less Hg^{II} (**Fig 1B, E**).
257 In relative terms, phototrophic cells reduced 12 to 15% of the initial Hg^{II} supplied whereas
258 fermentative cells reduced 31 to 40% (**Fig S2**).

259 Relative Hg^0 production in these experiments was lower, yet consistent with our previous
260 work, which showed fermentatively-grown cells reduced 15% more Hg^{II} than phototrophically-
261 grown cells, reducing between 60 to 75% of the initial Hg^{II} supplied (23). The relative amount of
262 Hg^0 production did not increase with higher Hg^{II} exposure (10 nM) versus previous experiments
263 (250 pM) (23). It is unlikely that the lower reduction rate observed in the experiments presented
264 here was due to the toxicity of 10 nM Hg supplied, given that *H. modesticaldum* grows well
265 under the same conditions at 50 times higher Hg concentrations (23). Instead, we suspect that the
266 lack of constant bubbling of the reactor may be responsible for the observed results. It is possible
267 that the accumulation of CO_2 in the bioreactor following organic carbon oxidation may compete
268 with Hg^{II} as an electron sink, decreasing the amount of Hg^0 produced. Inorganic carbon is
269 required for anaplerotic reactions that fulfill the biosynthetic needs of *H. modesticaldum* and CO_2
270 could have competed with Hg^{II} for reducing power, as previously shown (51). These results
271 could also be due to Hg^0 oxidation allowed by the increased residence time of Hg^0 in the reactor
272 afforded by the intermittent sparging, as has been observed in other anaerobes (52, 53).
273 Despite carefully controlling the growth conditions in our experiments, fermentative cells
274 from replicate #1 exhibited a lag phase of 12 hours (**Fig 1F**). Although this lag did not affect
275 final cell density, the slow-growing culture from replicate #1 initiated Hg^0 production earlier
276 than the culture in replicate #2 (**Fig 1E, F**). These results may be attributable to cells in replicate
277 #1 maintaining a higher Hg to cell ratio in the first 12 hours of the experiment, which suggests
278 that Hg is being reduced intracellularly in line with our previous work on Heliobacteria (23, 54).
279 Indeed, even at low initial densities, cells can maintain μM levels of intracellular reducing
280 power, which could be used to reduce nM levels of Hg^{II} (24).

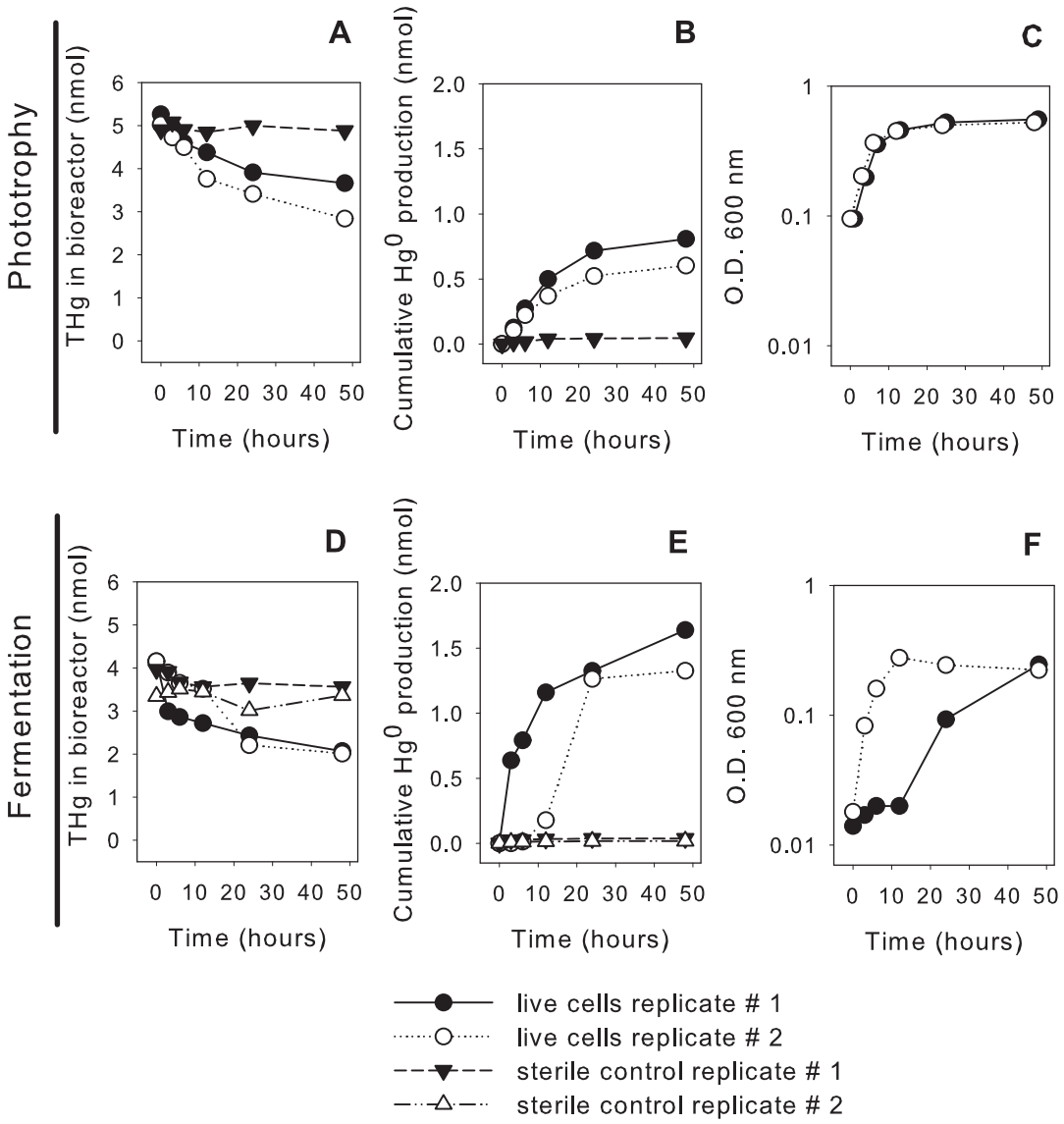

Figure 1: Total Hg and cumulative Hg^0 production by *H. modesticaldum* grown phototrophically and fermentatively. A, D THg for live cells and sterile controls without cells. **B, E** Cumulative Hg^0 production for live cells and sterile controls without cells. **C, F** Microbial growth as measured by O.D. 600 nm for live cells. 10 nM Hg was supplied in all experiments from the same stock (NIST 3133).

289 **Mass dependent fractionation during photosynthetic and fermentative growth**

290 Hg reduction in phototrophically-grown *H. modesticaldum* cultures resulted in consistent
291 positive MDF and negligible Δ^{199}Hg values (-0.01 ± 0.05 ‰, n = 28) in the reactant pool
292 indicating an absence of MIF (**Fig 2AB**, **Table S1,** and **Table S2**). Abiotic controls where light
293 was supplied showed minimal change in Hg isotope values related to both MDF and MIF,
294 confirming that Hg reduction and subsequent isotopic fractionation were predominantly driven
295 by cellular processes (**Fig 2A**, **Table S1,** and **Table S2**).

296 We attribute the lack of photochemical fractionation in our experiments to the low levels of
297 visible light and anoxic conditions employed in our setup. These conditions were designed to
298 minimize the amount of abiotic photoreduction observed compared to high energy UV light
299 sources (natural or controlled), such as those used to study Hg stable isotope fractionation in the
300 oxygenic phototrophic green alga *Isochrysis galbana* (41). In the study on *I. galbana*, the authors
301 suggested that UV-mediated production of free radical pairs, such as reactive oxygen species,
302 during photosynthetic electron transport contributed to MIF during Hg reduction (41). Such
303 reactions would likely be inhibited in our experimental setup because of the low energy
304 wavelengths characteristic of the irradiance we provided and the active removal of oxygen
305 required for the anoxygenic phototrophic growth of *H. modesticaldum*.

306 For phototrophically-grown cultures, the reactant pool $\delta^{202}Hg^{II}$ increased steadily over
307 time suggesting cells preferentially reduced lighter Hg^{II} (**Fig 2A**). A mirror trend was observed
308 for $\delta^{202}Hg^{0}$, which was depleted in $^{202}Hg^{0}$ at the beginning of the experiment, became enriched
309 with heavier isotopes as the reaction proceeded, and eventually approached the initial isotopic
310 composition of the NIST 3133 standard (approximately 0‰) (**Fig 2B**).

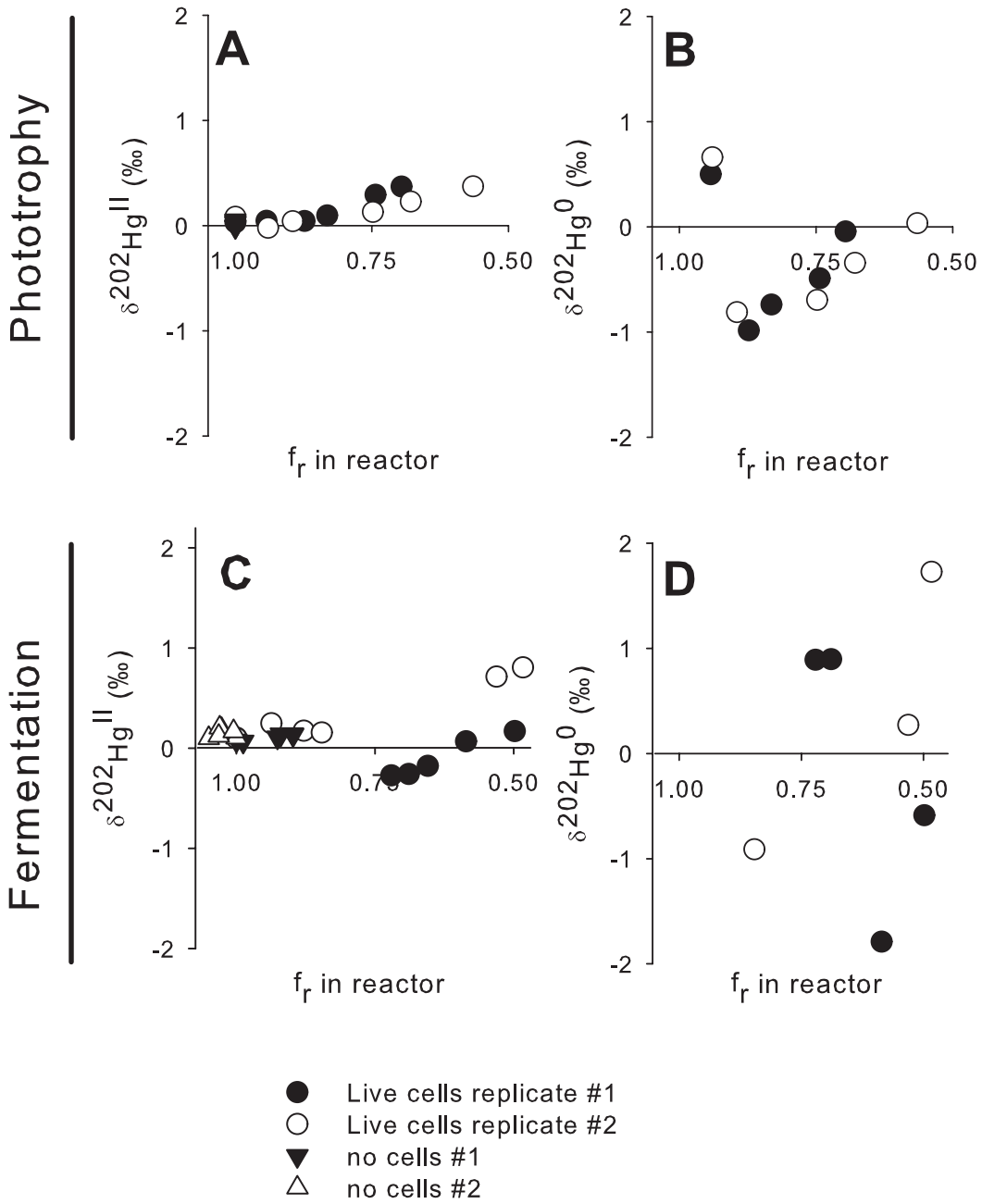

Figure 2: Mass dependent fractionation of ^{202}Hg in Hg^{II} (A, C) and Hg^{0} (B, D) during phototrophic and fermentative growth of *H. modesticaldum* and no cell controls. $\delta^{202}Hg$ values for Hg^{II} and Hg^{0} are plotted with respect to the fraction of remaining total inorganic Hg^{II} in the bioreactor. Insufficient Hg^{0} was recovered from the no cell controls and thus no results are displayed. 10 nM Hg was used in all experiments and Hg was supplied from the same stock (NIST 3133).

318 Curiously, the $\delta^{202}Hg^0$ for f_r = 0.94 at 3h in the two phototrophic live cell replicates showed
319 that the product pool was initially enriched with the $^{202}Hg^0$ isotope (**Fig 2B**). A similar pattern
320 has been observed in iron reducing bacteria that preferentially reduced heavier Fe^{III} (55), and the
321 model anaerobic Hg methylator and reducer *Geobacter sulfurreducens* PCA (37, 40). The most
322 recent work on *G. sulfurreducens* has shown that uptake of Hg selects for lighter Hg isotopes but
323 cells can also access an isotopically heavier pool of Hg^{II} from the dissolved phase (37). It is
324 possible that a similar process is occurring for phototrophically-grown *H. modesticaldum*
325 wherein cells access an isotopically heavier pool of Hg during equilibrium binding of Hg^{II} to the
326 outside of the cell, followed by an alternative uptake process that selects for lighter pools of Hg.
327 Based on these results, we included all time points in isotopic enrichment calculations for Hg^{II}
328 but omitted the 3h time point in calculations for Hg^0 given that other cellular fractionation
329 processes could be occurring (**Fig S3, Fig S4,** and **Table S3**).
330 Replicated experiments with fermentative cultures showed more variability with respect to
331 their fractionation patterns compared to phototrophic cultures, however positive MDF was
332 discernable (**Fig 2CD**). Replicate #1 showed an initial depletion in reactant pool $\delta^{202}Hg^{II}$ and
333 became progressively enriched with $^{202}Hg^{II}$ relative to the NIST 3133 standard suggesting lighter
334 isotopes were still preferentially reduced (**Fig 2C**). Note that the second $\delta^{202}Hg^{II}$ data point
335 available for replicate #1 occurs at f_r=0.72 due to the rapid rate of Hg^{II} reduction leading to
336 substantially less Hg remaining in the reactor (**Fig 1E** and **Fig 2C**). Results for replicate #2
337 further suggested that lighter Hg^{II} isotopes were preferentially reduced with $\delta^{202}Hg^{II}$ slightly
338 increasing at the beginning of the experiment before rising to a maximum of 0.81 ‰ between f_r =
339 0.85 at 12h and f_r = 0.48 at 48h (**Fig 2C**).

340 The trends for $\delta^{202}Hg^0$ in fermentative cultures mirrored what was observed for $\delta^{202}Hg^{II}$.
341 $\delta^{202}Hg^0$ from replicate #1 showed that the product pool was initially enriched with heavy $^{202}Hg^0$,
342 further suggesting cells may have accessed a readily bioavailable pool of heavy Hg^{II}, before
343 undergoing a pronounced depletion and progressive enrichment with heavy isotopes similar to
344 phototrophic cultures (**Fig 2BD**). In contrast, the $\delta^{202}Hg^0$ values for cells in replicate #2 suggest
345 that the product pool was depleted in $^{202}Hg^0$ before undergoing enrichment for heavier Hg^0,
346 isotopes reaching a maximum of 1.73 ‰ (**Fig 2D**). This enrichment in $^{202}Hg^0$ product exceeded
347 the initial composition of the NIST 3133 standard (0 ‰) suggesting fractionation deviated from
348 the predicted Rayleigh fractionation for Hg reduction (**Table S4**). Our observations in the Hg^0
349 product pool are similar to what has been reported for anaerobic cultures of *G. sulfurreducens*,
350 which produced product pools $\delta^{202}Hg$ values that exceeded the initial composition of the Hg^{II}
351 supplied during methylation (40). As previously mentioned, this type of enrichment in the
352 product pool could be driven by differences in the bioaccessible pools of Hg. Indeed, more
353 recent work with *G. sulfurreducen*s has reinforced the view that subcellular partitioning
354 processes can contribute to Hg isotope fractionation, although such changes were not detected at
355 the level of THg pool (37).
356 In our work, Hg reduction provided such a strong isotopic shift that we could detect
357 fractionation in the THg pool (**Fig 2**). However, we cannot discount the contributions of smaller
358 magnitude (<0.10 ‰) subcellular partitioning processes or the preferential utilization of different
359 intracellular Hg pools during Hg^{II} reduction that may more drastically affect the isotope values of
360 the Hg^0 product pool. Such processes could be driving the slight depletion of $^{202}Hg^{II}$ (-0.29 to -
361 0.18 ‰) early on for fermentative cells in replicate #1, where low cell densities may have
362 amplified uptake and adsorption-driven fractionation in comparison to experiments where cell

density increased by an order of magnitude over the same time frame (**Fig 1F** and **Fig 2C**). It is more challenging to discuss the contributions of such processes for replicate #2, where the low cumulative Hg^0 production at f_r = 0.94 and 0.88 (3h and 6h time points, respectively) precluded our ability to measure Hg^0 isotope fractionation (**Fig 1E** and **Table S2**). Despite this limitation, the high $\delta^{202}Hg^0$ value obtained for the final timepoint for replicate #2 reinforces that additional processes are contributing to fractionation during fermentative growth that warrant further exploration.

Our experimental results suggest that Hg^0 oxidation is not a major contributor at earlier stages of reduction (i.e. 3 to 12 hours) but may be contributing to isotope fractionation at later time points associated with longer Hg residence times in the reactor. Under phototrophic conditions, the measured values of $\delta^{202}Hg^{II}$ at 48h were isotopically heavier than predicted values, which suggests Hg^0 oxidation may be occurring (**Table S4**). Under fermentative conditions the potential contribution of Hg oxidation is unclear, since a consistent enrichment was not observed between replicates (**Table S4**). The variability in isotope results for later time points in both fermentative replicates suggests processes other than reduction may be occurring.

Although Hg^0 oxidation has never been observed in anoxygenic phototrophs, it has been observed in other model chemotrophic anaerobes (53). Recent work showed that thiol-bearing molecules preferentially oxidize heavy $^{202}Hg^0$, leading to negative MDF, in addition to a negative MIF signal (56). Although we did not observe any negative MDF or MIF in our experiments (**Table S1** and **Table S2**) to the extent seen in previous work (56), we acknowledge that such processes have the potential to contribute to net fractionation alongside internal partitioning related to uptake or adsorption processes.

386 The results presented in this work are an important first step to resolving the physiological
387 processes that drive anaerobic Hg transformations in *H. modesticaldum.* We demonstrate that
388 while biotic reduction of Hg during anoxygenic photosynthesis and fermentation drives Hg
389 isotope fractionation, other processes such as adsorption, cellular uptake, and equilibrium effects
390 have an important impact on the net isotope values observed. Our results suggest that the extent
391 to which these additional processes affect isotope fractionation is tightly coupled to cellular Hg
392 availability and the physiological state of cell cultures. These biological controls and overlapping
393 Hg reactions are key to elucidating the Hg isotope signature associated with environmental
394 processes, such as reduction. Bearing these nuances in mind, we aim to carry out additional
395 experiments that assess the contributions of uptake, adsorption, and redox transformations to the
396 net Hg isotope fractionation associated with anaerobic Hg reduction.
397
398 **Comparing enrichment factors for abiotic and biotic Hg transformations**
399 Our initial motivation for this study was to test if phototrophic and fermentative Hg reduction led
400 to different isotope enrichment factors and establish whether different underlying processes
401 supported different metabolic Hg reduction pathways. When comparing ε values, which are used
402 as an index to distinguish between different isotope fractionation processes, we obtained average
403 enrichment factors using the ratio of product to reactant ($\varepsilon_{p/r}$) ± 2 standard deviations (2SD) for
404 MDF in the reactant pool Hg^{II} of -0.80 ± 0.56 ‰, for anoxygenic photosynthesis (ε_{AP}), and -1.15
405 ± 0.48 ‰, for fermentation (ε_{FM}) (**Fig 3, Fig S3, Table S3,** and **Table S5**). The enrichment factor
406 could not be calculated using the product Hg^0 pool for fermentative cultures, and ε was
407 overestimated in phototrophic cultures (-2.86 ± 1.32 ‰), likely due to challenges in obtaining
408 analytical replicates of gaseous Hg^0 and quantitatively collecting this pool (57) (**Fig S4** and

409 **Table S3**). The small difference between ε_{AP} and ε_{FM} (i.e. 0.35 ‰) could suggest common
410 controls for Hg reduction during photosynthesis and fermentation. However, we acknowledge
411 that we could not effectively test our hypothesis due to the variability observed in replicated
412 fermentative experiments where the cell populations used were in different physiological states,
413 as supported by the growth curves (**Fig 1F**). Despite this limitation, our work demonstrates that
414 net isotopic enrichment stems from a combination of multiple processes most likely affected by
415 Hg transport (e.g. adsorption, uptake, and efflux) that would occur regardless of the intracellular
416 transformations in question.

417 Given that this is the first report of isotope enrichment signatures for Hg reduction during
418 anoxygenic photosynthesis and fermentation, there is value in comparing the signatures from this
419 work to previously published data. This comparison can help better understand the physiological
420 processes that control microbial Hg transformations and advance Hg isotope applications. For
421 convenience, we have presented the enrichment values for our replicated experiments separately
422 in **Figure 3** and provide data compiled from the literature alongside any manipulations carried
423 out to facilitate comparisons in **Table S5**.

424 The isotopic enrichment observed for both metabolisms tested in *H. modesticaldum* falls
425 between the values observed for abiotic and microbial Hg reduction pathways (**Fig 3** and **Table**
426 **S5**). The isotopic enrichment for MDF observed for replicated experiments with phototrophic *H.*
427 *modesticaldum* is slightly lower or equal to photoreduction in the presence of dissolved organic
428 carbon (-1.00 to -0.60 ‰ vs -0.60 ± 0.20 ‰, respectively) (32), but higher than photoreduction in
429 the presence of marine exudates and UVB light (-1.00 to -0.60 ‰ vs -1.47 ‰, respectively) (41)
430 (**Fig 3** and **Table S5**). When comparing Hg reduction in the anoxygenic phototroph *H.*
431 *modesticaldum* to the oxygenic phototrophic green alga *I. galbana*, the isotopic enrichment

observed is slightly lower or equal, depending on the treatment in question (-1.00 to -0.60 ‰ vs -0.14 for high UV and -0.60 ‰ for low UV, respectively) (41) (**Fig 3** and **Table S5**). Though the similar ε value of the low UV treatment suggests anoxygenic and oxygenic photosynthetic Hg reduction share a common physiological pathway, the presence of MIF in *I. galbana* due to free radical generation within the cell rules out this possibility (41). (**Table S1**). Thus, Hg reduction during anoxygenic photosynthetic Hg reduction could be distinguished from other photo-induced reduction pathways, which display MIF in the reactant Hg^{II} pool (60).

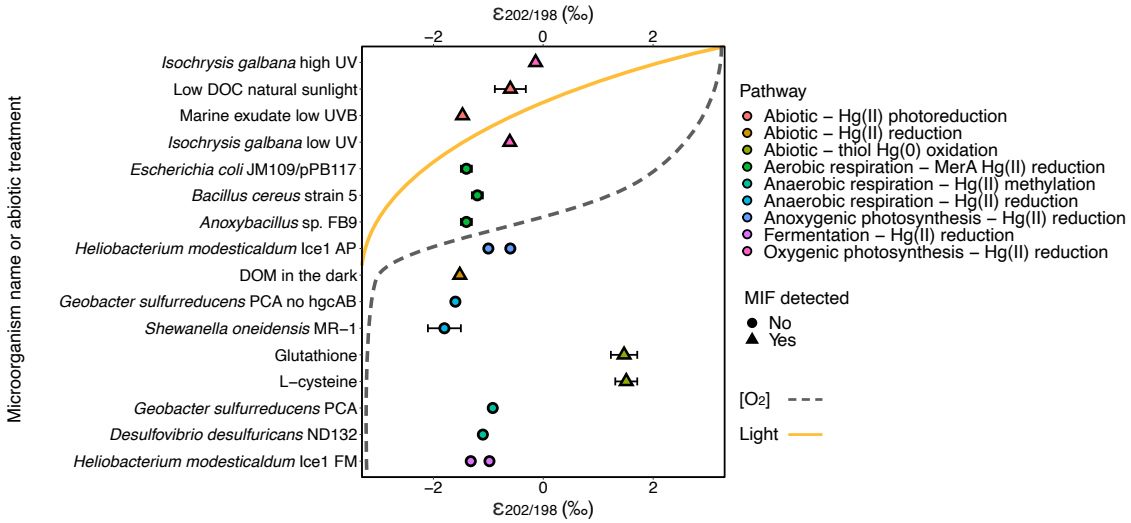

Figure 3: Compilation of isotopic enrichment factors (ε) associated with mass dependent fractionation for abiotic and biotic Hg transformations. Hg transformation pathways are denoted by colours and the detection of mass-independent fractionation (MIF) is denoted by different shapes. Note that the data originating from this work is presented as separate replicates to emphasize the range of ε that observations fall within. For all other data, error bars denote 2 standard deviations for studies where this data was available. In the event that data was presented as a standard error between replicated experiments, standard deviation was calculated based on the sample size indicated in each study. Abbreviations on the y-axis denote the following: UV (ultraviolet light), DOC (dissolved organic carbon), DOM (dissolved organic matter), AP (anoxygenic photosynthesis), ΔhgcAB (no *hgcAB* gene cluster), and FM (fermentation). The curves in this figure represent gradients for light and oxygen (O_2). The values in this figure were obtained from the following studies: Abiotic – Hg(II) photoreduction (32, 41); abiotic – Hg(II) reduction (58); abiotic – thiol Hg(0) oxidation (56); aerobic respiration - MerA Hg(II) reduction (34, 36); anaerobic respiration – Hg(II) methylation (40); anaerobic respiration – Hg(II) reduction (36, 37); anoxygenic photosynthesis – Hg(II) reduction (this study); fermentation – Hg(II) reduction (this study); oxygenic photosynthesis – Hg(II) reduction (41). The raw data in this figure are in **Table S5**.

457 When compared with previous work on microbial Hg reduction in pure cultures, the isotopic
458 enrichment observed for phototrophically-grown *H. modesticaldum* was higher than what has
459 previously been reported for aerobic *mer*-mediated reduction and Hg reduction during anaerobic
460 respiration (-1.00 to -0.60 ‰ vs -1.80 to -1.20 ‰, respectively) (34, 36, 37) (**Fig 3** and **Table**
461 **S5**). Interestingly, the isotopic enrichment observed in fermentatively-grown *H. modesticaldum*
462 (-1.32 to -0.98 ‰) was closer to aerobic *mer*-mediated reduction (-1.40 to -1.20 ‰) (34) than to
463 Hg reduction during anaerobic respiration in *Shewanella oneidensis* MR-1 and a modified strain
464 of *G. sulfurreducens* PCA incapable of Hg methylation (-1.80 to -1.60 ‰) (**Fig 3** and **Table S5**)
465 (36, 37). The enrichment values reported for dark abiotic Hg^{II} reduction catalyzed by dissolved
466 organic matter (DOM) are slightly lower compared to fermentative Hg^{II} reduction (-1.32 to -0.98
467 ‰ vs -1.52‰). Similar to what was mentioned for photoreduction previously, DOM-mediated
468 transformations display varying degrees of MIF such that fermentative Hg^{II} reduction could be
469 distinguished from DOM-mediated Hg reduction in the dark (**Fig 3** and **Table S5**) (58). An
470 additional line of evidence supporting that Hg^0 oxidation is unlikely to be contributing to the
471 isotope signature observed in our system are the ε values for thiol mediated Hg^0 oxidation in the
472 dark. These values are considerably larger than what we observed for *H. modesticaldum* (1.51 ±
473 0.20 ‰ for cysteine and 1.47 ± 0.24 ‰ for glutathione) (**Fig 3** and **Table S5**) (56)
474 These comparisons illustrate that isotopic enrichment for microbial Hg reduction
475 pathways that only display MDF fall within a narrow range (i.e. -0.60 to -1.80 ‰) (**Fig 3** and
476 **Table S5**). We find this to be a strikingly small difference given the ecological diversity of the
477 model organisms and variety of growth conditions used to study microbial Hg reduction. The
478 similar ε values reported for fermentation in this study and the *mer* operon are also noteworthy,

479 as they suggest nearly identical isotope enrichment can occur in aerobes harbouring dedicated
480 enzymatic machinery to reduce Hg and anaerobes where *mer*-based strategies are largely absent.
481 Our study also shows that similar isotopic enrichment can be observed for different
482 anaerobic Hg transformations. The anaerobic Hg methylating chemotrophs *G. sulfurreducens*
483 PCA and *Desulfovibrio desulfuricans* ND132 displayed ε signatures (i.e. -0.92 and -1.10 ‰,
484 respectively) that fall within the range of ε values we report in our study (i.e. -1.32 to -0.60 ‰)
485 (**Fig 3** and **Table S5**) (40). The similarity in enrichment signatures suggests that common
486 processes may affect the delivery of inorganic Hg substrates to intracellular sites independently
487 of the Hg transformations in question. Although it is outside of the scope of the current study,
488 identifying the nature of these processes may provide insights into similar controls that exist for
489 Hg uptake and transformation in anaerobes.
490 Our work showcases the strengths but also the challenges of using isotope fractionation-
491 based approaches to decipher cryptic Hg cycling pathways. To illustrate the challenges of using
492 isotopes to track Hg cycling pathways in the environment, we visualized our comparison of ε
493 values in the context of a vertically redox stratified habitat (e.g. a water column) (**Fig 3**).
494 Through Hg stable isotope fractionation, we can distinguish between abiotic and biotic redox
495 reaction pathways that control Hg's availability in methylation hotspots, such as the limit of the
496 photic zone, on the bases of MIF signatures associated with photochemical and DOM-mediated
497 reactions. In contrast, teasing apart biological pathways that contribute to the net isotope
498 signature of Hg^{II} in the environment is more challenging because competing MDF processes
499 occur in both dark and photo-mediated pathways where Hg^{II} is a reactant (e.g. reduction and
500 methylation) and a product (e.g. demethylation and oxidation). This overlap makes it difficult to
501 translate $\delta^{202}Hg$ values observed under controlled conditions that are sensitive to changes in

502 cellular physiology to environments where pools of bioavailable Hg are not homogenous due to
503 variable mixing.
504

505 **CONCLUSION**

506 In this study we provide the first reports of MDF associated with Hg reduction during
507 anoxygenic photosynthesis and fermentation. We show that isotopic enrichment during
508 anoxygenic phototrophic Hg reduction leads to an intermediate fractionation process that lies
509 between photochemical reactions and dark microbial Hg reduction. We also show that
510 fermentative Hg reduction leads to isotopic enrichment that is similar to aerobic *mer*-mediated
511 reduction. Although we could not discern whether dedicated physiological processes support Hg
512 reduction during anoxygenic photosynthesis and fermentation, our study shows that isotopes are
513 well-suited to teasing apart the complex interwoven processes that drive microbe-mediated Hg
514 transformations and highlighting common processes that control Hg bioavailability to microbes.
515 In future work, it will be important to isolate the different steps involved in Hg uptake
516 and transformation by rigorously controlling Hg availability and cellular physiology. Leveraging
517 molecular tools alongside isotopes will be a useful strategy to address these knowledge gaps and
518 the recent availability of genetically tractable *H. modesticaldum* deletion mutants offers a
519 promising means to do so (61). In that regard, gene deletion approaches targeting redox-active
520 enzymes could be used to characterize the physiological components contributing directly to Hg^{II}
521 reduction, whereas targeting homologues for proteins involved in Hg uptake in other model
522 anaerobes could be the key to identifying entry routes for Hg into *H. modesticaldum* (62, 63). By
523 combining molecular tools with isotope-based approaches to study anaerobic Hg reduction, we
524 may finally be able characterize the contributions of such pathways to the global Hg cycle in

present day environments and historical archives (e.g. sediment records). Such studies would help better understand the ecological conditions that gave rise to the evolution of anaerobic Hg redox cycling pathways prior to the acquisition of dedicated Hg detoxification strategies such as the *mer* operon.

ACKNOWLEDGMENTS

Our work was funded by NSERC Discovery and Accelerator grants, CFI funding to AJP and NSERC graduate scholarship to DSG. Instrumentation and lab operations for Hg isotope analyses were supported by the USGS Toxic Substances Hydrology Program. Any use of trade, firm, or product names is for descriptive purposes only and does not imply endorsement by the U.S. Government.

AUTHOR CONTRIBUTIONS

DSG, AJP, SEJ and MTT designed all experiments; DSG and NCL carried out bioreactor experiments and data analyses; SEJ and MTT carried out total Hg and stable isotope analyses; DSG, AJP, SEJ and MTT wrote the manuscript.

REFERENCES

1. Selin NE. 2009. Global Biogeochemical Cycling of Mercury: A Review. Annual Review of Environment and Resources 34:43-63.
2. Parks JM, Johs A, Podar M, Bridou R, Hurt Jr RA, Smith SD, Tomanicek SJ, Qian Y, Brown SD, Brandt CC, Palumbo AV, Smith JC, Wall JD, Elias DA, Liang L. 2013. The genetic basis for bacterial mercury methylation. Science 339:1332-1335.
3. Fleming EJ, Mack EE, Green PG, Nelson DC. 2006. Mercury methylation from unexpected sources: Molybdate-inhibited freshwater sediments and an iron-reducing bacterium. Applied and Environmental Microbiology 72:457-464.
4. Han S, Narasingarao P, Obraztsova A, Gieskes J, Hartmann AC, Tebo BM, Allen EE, Deheyn DD. 2010. Mercury speciation in marine sediments under sulfate-limited conditions. Environmental Science and Technology 44:3752-3757.
5. Podar M, Gilmour CC, Brandt CC, Soren A, Brown SD, Crable BR, Palumbo AV, Somenahally AC, Elias DA. 2015. Global prevalence and distribution of genes and microorganisms involved in mercury methylation. Science Advances 1:1-13.
6. Schartup AT, Balcom PH, Soerensen AL, Gosnell KJ, Calder RS, Mason RP, Sunderland EM. 2015. Freshwater discharges drive high levels of methylmercury in Arctic marine biota. Proceedings of the National Academy of Sciences of the United States of America 112:11789-94.
7. Hsu-Kim H, Kucharzyk KH, Zhang T, Deshusses MA. 2013. Mechanisms regulating mercury bioavailability for methylating microorganisms in the aquatic environment: a critical review. Environmental Science and Technology 47:2441-56.
8. Gustin MS, Biester H, Kim CS. 2002. Investigation of the light-enhanced emission of mercury from naturally enriched substrates. Atmospheric Environment 36:3241-3254.
9. Amyot M, Lean D, Mierle G. 1997. Photochemical formation of volatile mercury in high Arctic lakes. Environmental Toxicology and Chemistry 16:2054-2063.
10. Whalin L, Kim EH, Mason R. 2007. Factors influencing the oxidation, reduction, methylation and demethylation of mercury species in coastal waters. Marine Chemistry 107:278-294.
11. Poulain AJ, Amyot M, Findlay D, Findlay S, Telor S, Barkay T, Hintelmann H, Amyot M, Findlay D. 2011. Biological and photochemical production of dissolved gaseous mercury in a boreal lake. Limnology 49:2265-2275.
12. Carpi A, Lindberg SE. 1997. Sunlight-mediated emission of elemental mercury from soil amended with municipal sewage sludge. Environmental Science and Technology 31:2085-2091.
13. Vandal GM, Fitzgerald WF, Rolfhus KR, Lamborg CH. 1995. Modeling the elemental mercury cycle in Pallette Lake, Wisconsin, USA. Water, air, and soil pollution 80:529-538.
14. Zhang H, Lindberg SE. 2001. Sunlight and iron(III)-induced photochemical production of dissolved gaseous mercury in freshwater. Environmental Science and Technology 35:928-935.
15. Zhang H. 2006. Photochemical redox reactions of mercury, p 37-79. *In* Atwood DA (ed), Recent Developments in Mercury Science, vol 120.

16. O'Driscoll NJ, Lean DRS, Loseto LL, Carignan R, Siciliano SD. 2004. Effect of dissolved organic carbon on the photoproduction of dissolved gaseous mercury in lakes: Potential impacts of forestry. Environmental Science and Technology 38:2664-2672.
17. Gu B, Bian Y, Miller CL, Dong W, Jiang X, Liang L. 2011. Mercury reduction and complexation by natural organic matter in anoxic environments. Proceedings of the National Academy of Sciences of the United States of America 108:1479-1483.
18. Wiatrowski HA, Das S, Kukkadapu R, Ilton ES, Barkay T, Yee N. 2009. Reduction of Hg(II) to Hg(0) by magnetite. Environmental Science and Technology 43:5307-5313.
19. Bone SE, Bargar JR, Sposito G. 2014. Mackinawite (FeS) reduces mercury(II) under sulfidic conditions. Environmental Science and Technology 48:10681-10689.
20. Wiatrowski HA, Ward PM, Barkay T. 2006. Novel reduction of mercury(II) by mercury-sensitive dissimilatory metal reducing bacteria. Environmental Science and Technology 40:6690-6696.
21. Lu X, Liu Y, Johs A, Zhao L, Wang T, Yang Z, Lin H, Elias DA, Pierce EM, Liang L, Barkay T, Gu B. 2016. Anaerobic mercury methylation and demethylation by *Geobacter bemidjiensis* Bem. Environmental Science and Technology 50:4366-4373.
22. Lin H, Morrell-Falvey JL, Rao B, Liang L, Gu B. 2014. Coupled mercury-cell sorption, reduction, and oxidation on methylmercury production by *Geobacter sulfurreducens* PCA. Environmental Science and Technology 48:11969-11976.
23. Grégoire DS, Lavoie NC, Poulain AJ. 2018. Heliobacteria reveal fermentation as a key pathway for mercury reduction in anoxic environments. Environmental Science and Technology 52:4145-4153.
24. Grégoire DS, Poulain AJ. 2016. A physiological role for Hg(II) during phototrophic growth. Nature Geoscience 9:121-125.
25. Barkay T, Kritee K, Boyd E, Geesey G. 2010. A thermophilic bacterial origin and subsequent constraints by redox, light and salinity on the evolution of the microbial mercuric reductase. Environmental Microbiology 12:2904-2917.
26. Grégoire DS, Poulain AJ. 2014. A little bit of light goes a long way: the role of phototrophs on mercury cycling. Metallomics 6:396-407.
27. Poulin BA, Aiken GR, Nagy KL, Monceau A, Krabbenhoft DP, Ryan JN. 2016. Mercury transformation and release differs with depth and time in a contaminated riparian soil during simulated flooding. Geochimica Et Cosmochimica Acta 176:118-138.
28. Bouffard A, Amyot M. 2009. Importance of elemental mercury in lake sediments. Chemosphere 74:1098-1103.
29. Grégoire DS, Poulain AJ. 2018. Shining light on recent advances in microbial mercury cycling. FACETS 3:858-879.
30. Blum JD, Sherman LS, Johnson MW. 2014. Mercury Isotopes in Earth and Environmental Sciences. Annual Review of Earth and Planetary Sciences 42:249-269.
31. Zheng W, Gilleaudeau GJ, Kah LC, Anbar AD. 2018. Mercury isotope signatures record photic zone euxinia in the Mesoproterozoic ocean. Proceedings of the National Academy of Sciences 115:10594-10599.
32. Bergquist BA, Blum JD. 2007. Mass-dependent and -independent fractionation of Hg isotopes by photoreduction in aquatic systems. Science 318:417-420.
33. Bergquist BA, Blum JD. 2009. The odds and evens of mercury isotopes: Applications of mass-dependent and mass-independent isotope fractionation. Elements 5:353-357.

34. Kritee K, Blum JD, Johnson MW, Bergquist BA, Barkay T. 2007. Mercury stable isotope fractionation during reduction of Hg(II) to Hg(0) by mercury resistant microorganisms. Environmental Science and Technology 41:1889-1895.
35. Kritee K, Barkay T, Blum JD. 2009. Mass dependent stable isotope fractionation of mercury during mer mediated microbial degradation of monomethylmercury. Geochimica et Cosmochimica Acta 73:1285-1296.
36. Kritee K, Blum JD, Barkay T. 2008. Mercury stable isotope fractionation during reduction of Hg(II) by different microbial pathways. Environmental Science and Technology 42:9171-9177.
37. Wang Y, Janssen SE, Schaefer JK, Yee N, Reinfelder JR. 2020. Tracing the Uptake of Hg(II) in an Iron-Reducing Bacterium Using Mercury Stable Isotopes. Environmental Science & Technology Letters doi:10.1021/acs.estlett.0c00409.
38. Rodríguez-González P, Epov VN, Bridou R, Tessier E, Guyoneaud R, Monperrus M, Amouroux D. 2009. Species-specific stable isotope fractionation of mercury during Hg(II) methylation by an anaerobic bacteria (*Desulfobulbus propionicus*) under dark conditions. Environmental Science and Technology 43:9183-9188.
39. Perrot V, Bridou R, Pedrero Z, Guyoneaud R, Monperrus M, Amouroux D. 2015. Identical Hg isotope mass dependent fractionation signature during methylation by sulfate-reducing bacteria in sulfate and sulfate-free environment. Environmental Science and Technology 49:1365-1373.
40. Janssen SE, Schaefer JK, Barkay T, Reinfelder JR. 2016. Fractionation of mercury stable isotopes during microbial methylmercury production by iron- and sulfate-reducing bacteria. Environmental Science and Technology 50:8077-8083.
41. Kritee K, Motta LC, Blum JD, Tsui MT-K, Reinfelder JR. 2018. Photomicrobial visible light-induced magnetic mass independent fractionation of mercury in a marine microalga. ACS Earth and Space Chemistry 2:432-440.
42. Zhang H, Feng X, Larssen T, Qiu G, Vogt RD. 2010. In Inland China, Rice, Rather than Fish, Is the Major Pathway for Methylmercury Exposure. Environmental Health Perspectives 118:1183-1188.
43. Asao M, Madigan MT. 2010. Taxonomy, phylogeny, and ecology of the heliobacteria. Photosynthesis Research 104:103-111.
44. Madigan MT. 2006. The family Heliobacteriaceae, p 951-964. *In* Dworkin M, Falkow S, Rosenberg E, Schleifer K-H, Stackenbrandt E (ed), The Prokaryotes: Vol 4. Springer, New York, NY.
45. Girija KR, Vinay B, Sasikala C, Ramana CV. 2010. Novel heliobacteria of a few semi-arid tropical soils. Indian Journal of Microbiology 50:17-20.
46. EPA U. 2002. Method 1631, Revision E: Mercury in water by oxidation, purge and trap, and cold vapor atomic fluorescence spectrometry. US Environmental Protection Agency Washington, DC.
47. Janssen SE, Lepak RF, Tate MT, Ogorek JM, DeWild JF, Babiarz CL, Hurley JP, Krabbenhoft DP. 2019. Rapid pre-concentration of mercury in solids and water for isotopic analysis. Analytica Chimica Acta 1054:95-103.
48. Yin R, Krabbenhoft DP, Bergquist BA, Zheng W, Lepak RF, Hurley JP. 2016. Effects of mercury and thallium concentrations on high precision determination of mercury isotopic composition by Neptune Plus multiple collector inductively coupled plasma mass spectrometry. Journal of Analytical Atomic Spectrometry 31:2060-2068.

676 49. Blum JD, Bergquist BA. 2007. Reporting of variations in the natural isotopic
677 composition of mercury. Analytical and Bioanalytical Chemistry 388:353-359.
678 50. Lepak RF, Yin R, Krabbenhoft DP, Ogorek JM, DeWild JF, Holsen TM, Hurley JP.
679 2015. Use of stable isotope signatures to determine mercury sources in the Great Lakes.
680 Environmental Science & Technology Letters 2:335-341.
681 51. Tang KH, Feng XY, Zhuang WQ, Alvarez-Cohen L, Blankenship RE, Tang YJ. 2010.
682 Carbon Flow of Heliobacteria Is Related More to Clostridia than to the Green Sulfur
683 Bacteria. Journal of Biological Chemistry 285:35104-35112.
684 52. Colombo MJ, Ha J, Reinfelder JR, Barkay T, Yee N. 2013. Anaerobic oxidation of Hg(0)
685 and methylmercury formation by *Desulfovibrio desulfuricans* ND132. Geochimica et
686 Cosmochimica Acta 112:166-177.
687 53. Colombo MJ, Ha J, Reinfelder JR, Barkay T, Yee N. 2014. Oxidation of Hg(0) to Hg(II)
688 by diverse anaerobic bacteria. Chemical Geology 363:334-340.
689 54. Lavoie NC, Grégoire DS, Stenzler BR, Poulain AJ. 2020. Reduced sulphur sources
690 favour HgII reduction during anoxygenic photosynthesis by Heliobacteria. Geobiology
691 18:70-79.
692 55. Icopini GA, Anbar AD, Ruebush SS, Tien M, Brantley SL. 2004. Iron isotope
693 fractionation during microbial reduction of iron: The importance of adsorption. Geology
694 32:205-208.
695 56. Zheng W, Demers JD, Lu X, Bergquist BA, Anbar AD, Blum JD, Gu B. 2019. Mercury
696 stable isotope fractionation during abiotic dark oxidation in the presence of thiols and
697 natural organic matter. Environmental Science and Technology 53:1853-1862.
698 57. Kritee K, Blum JD, Reinfelder JR, Barkay T. 2013. Microbial stable isotope fractionation
699 of mercury: A synthesis of present understanding and future directions. Chemical
700 Geology 336:13-25.
701 58. Zheng W, Hintelmann H. 2010. Nuclear field shift effect in isotope fractionation of
702 mercury during abiotic reduction in the absence of light. The Journal of Physical
703 Chemistry A 114:4238-4245.
704 59. Tang KH, Yue H, Blankenship RE. 2010. Energy metabolism of Heliobacterium
705 modesticaldum during phototrophic and chemotrophic growth. Bmc Microbiology 10.
706 60. Motta LC, Kritee K, Blum JD, Tsz-Ki Tsui M, Reinfelder JR. 2020. Mercury isotope
707 fractionation during the photochemical reduction of Hg(II) coordinated with organic
708 ligands. The Journal of Physical Chemistry A 124:2842-2853.
709 61. Baker PL, Orf GS, Kevershan K, Pyne ME, Bicer T, Redding KE. 2019. Using the
710 endogenous CRISPR-Cas system of *Heliobacterium modesticaldum* to delete the
711 photochemical reaction center core subunit gene. Applied and Environmental
712 Microbiology 85:e01644-19.
713 62. Stenzler B, Hinz A, Ruuskanen M, Poulain AJ. 2017. Ionic strength differentially affects
714 the bioavailability of neutral and negatively charged inorganic Hg complexes.
715 Environmental Science and Technology 51:9653-9662.
716 63. Schaefer JK, Szczuka A, Morel FM. 2014. Effect of divalent metals on Hg(II) uptake and
717 methylation by bacteria. Environmental Science and Technology 48:3007-13.
718 64. Ruuskanen MO, Aris-Brosou S, Poulain AJ. 2020. Swift evolutionary response of
719 microbes to a rise in anthropogenic mercury in the Northern Hemisphere. The ISME
720 Journal 14:788-800.

721

722 **FIGURE CAPTIONS**

723

724 **Figure 1: Total Hg and cumulative Hg^0 production by *H. modesticaldum* grown**

725 **phototrophically and fermentatively. A, D** THg for live cells and sterile controls without cells.

726 **B, E** Cumulative Hg^0 production for live cells and sterile controls without cells. **C, F** Microbial

727 growth as measured by O.D. 600 nm for live cells. 10 nM Hg was supplied in all experiments

728 from the same stock (NIST 3133).

729

730 **Figure 2: Mass dependent fractionation of ^{202}Hg in Hg^{II} (A, C) and Hg^0 (B, D) during**

731 **phototrophic and fermentative growth of *H. modesticaldum* and no cell controls**. $\delta^{202}Hg$

732 values for Hg^{II} and Hg^0 are plotted with respect to the fraction of remaining total inorganic Hg^{II}

733 in the bioreactor. Insufficient Hg^0 was recovered from the no cell controls and thus no results are

734 displayed. 10 nM Hg was used in all experiments and Hg was supplied from the same stock

735 (NIST 3133).

736

737 **Figure 3: Compilation of isotopic enrichment factors (ε) associated with mass dependent**

738 **fractionation for abiotic and biotic Hg transformations.** Hg transformation pathways are

739 denoted by colours and the detection of mass-independent fractionation (MIF) is denoted by

740 different shapes. Note that the data originating from this work is presented as separate replicates

741 to emphasize the range of ε that observations fall within. For all other data, error bars denote 2

742 standard deviations for studies where this data was available. In the event that data was presented

743 as a standard error between replicated experiments, standard deviation was calculated based on

744 the sample size indicated in each study. Abbreviations on the y-axis denote the following: UV

745 (ultraviolet light), DOC (dissolved organic carbon), DOM (dissolved organic matter), AP

746 (anoxygenic photosynthesis), ΔhgcAB (no *hgcAB* gene cluster), and FM (fermentation). The
747 curves in this figure represent gradients for light and oxygen (O_2). The values in this figure were
748 obtained from the following studies: Abiotic – Hg(II) photoreduction (32, 41); abiotic – Hg(II)
749 reduction (58); abiotic – thiol Hg(0) oxidation (56); aerobic respiration - MerA Hg(II) reduction
750 (34, 36); anaerobic respiration – Hg(II) methylation (40); anaerobic respiration – Hg(II)
751 reduction (36, 37); anoxygenic photosynthesis – Hg(II) reduction (this study); fermentation –
752 Hg(II) reduction (this study); oxygenic photosynthesis – Hg(II) reduction (41). The raw data in
753 this figure are in **Table S5**.
754

755 ## SUPPORTING INFORMATION CAPTIONS

756 **Figure S1:** Schematic of the bioreactor setup used to measure Hg stable isotope fractionation for
757 Hg^{II} and Hg^{0} during the anaerobic reduction of Hg^{II}.
758

759 **Figure S2**: **Total Hg mass balance for isotope fractionation experiments under**
760 **phototrophic and fermentative growth conditions.** The average recovery across all
761 experiments was 94.40 ± 9.50 % (n=7) and is shown by the dashed red line.

762

763 **Figure S3: Mass dependent fractionation of $^{202}Hg^{II}$ in phototrophically- (A, B) and**
764 **fermentatively-grown (C, D) *H. modesticaldum*.** $\delta^{202}Hg$ values for Hg^{II} are plotted as open
765 system Rayleigh fractionation models with $\ln(R/R_0)$ vs $\ln(f_r)$. The amount of Hg^{II} remaining in
766 the reactor was used to calculate f_r (see Methods). The 0h time point for fermentative live cells
767 replicate #1 was omitted from the regression fitted to the data for Hg^{II} (C) as this suggested an
768 alternative process was contributing to isotopic fractionation earlier on in the experiment.

Figure S4: Mass dependent fractionation of $^{202}Hg^0$ in phototrophically- (A, B) and fermentatively- (C, D) grown *H. modesticaldum*. δ^{202}Hg values for Hg^0 are plotted as open system Rayleigh fractionation models with $\ln(R/R_0)$ vs $\ln(f_r)$. The amount of Hg^{II} remaining in the reactor was used to calculate f_r (see Methods). The 3h time point for phototrophic cells in replicates #1 and 2 were omitted from the regression fitted to the data for Hg^0 (A, B) as this suggested an alternative process was contributing to isotopic fractionation earlier on in the experiment. No significant regressions were obtained for fermentative cells.

Table S1: Total Hg concentrations and Hg isotope ratios for the reactant pool Hg^{II} in phototrophic and fermentative experiments. Each line corresponds to an individual sample and technical duplicates were taken for each time point. Std represents the standard deviation from analytical replicates on the MC-ICP-MS. Abbreviations denote Metabo. = metabolism; Photo. = phototrophy; Ferm. = fermentation; Treat. = treatment; Hg conc. = Hg concentration, rep = replicate; Avg = average; Std = standard deviation; ctl = control, MED = medium. δ^{202}Hg values in **bold** denote those that deviate substantially from the composition of the NIST 3133 standard in medium spiked controls.

Table S2: Total Hg concentrations and Hg isotope ratios for the Hg^0 pool in phototrophic and fermentative experiments. Each line corresponds to the Hg present on two gold traps used to sample each time point in parallel. Std represents the standard deviation from analytical replicates on the MC-ICP-MS. Abbreviations denote the following: Metabo. = metabolism; Photo. =phototrophy; Ferm. = fermentation; Treat. = treatment; Hg conc. = Hg concentration, rep = replicate; Avg = average; Std = standard deviation.

Table S3: Summary of regression models for mass dependent fractionation of $^{202}Hg^{II}$ and $^{202}Hg^{0}$ in phototrophically- and fermentatively-grown *H. modesticaldum* cultures. P-values for regressions that displayed a significant ($p<0.05$) fit are shown in **bold**.

Table S4: Comparison of measured and calculated isotope fractionation values for the reactant pool of Hg^{II} using a mass balance approach. Measured values of Hg concentration and $\delta^{202}Hg$ are represented as an average of replicates from experiments presented in Tables S1 and S2. Predicted values for media were obtained using the equations outlined for mass balance calculations. Differences between the measured and predicted values that are substantially greater than the analytical variability of measurements (2SD = 0.08) are shown in **bold**. The asterisk for the 48HR timepoint in fermentative replicate #2 indicates that an average value was not taken due to the inability to analyze the replicate samples for Hg isotopes. Abbreviations denote Photo. = phototrophic, Ferm. = fermentation, rep = replicates, Avg. = average, Pred. = predicted.

Table S5: Comparison of enrichment factors and measures of variability used in this study and the original cited work. Abbreviations: SD = standard deviation, SE = standard error, p = product, r = reactant, Ox. = oxygenic, Anox. = anoxygenic, PS = photosynthesis.